PNAS

Anion efflux mediates transduction in the hair cells of the zebrafish lateral line

Elias T. Lunsford[a,b,1] (ID), Yuriy V. Bobkov[a,1] (ID), Brandon C. Ray[a], James C. Liao[a,2] (ID), and James A. Strother[a,2] (ID)

Hair cells are the principal sensory receptors of the vertebrate auditory system, where they transduce sounds through mechanically gated ion channels that permit cations to flow from the surrounding endolymph into the cells. The lateral line of zebrafish has served as a key model system for understanding hair cell physiology and development, often with the belief that these hair cells employ a similar transduction mechanism. In this study, we demonstrate that these hair cells are exposed to an unregulated external environment with cation concentrations that are too low to support transduction. Our results indicate that hair cell excitation is instead mediated by a substantially different mechanism involving the outward flow of anions. Further investigation of hair cell transduction in a diversity of sensory systems and species will likely yield deep insights into the physiology of these unique cells.

sensory transduction | hair cells | auditory | vestibular | chloride

Vertebrate hair cells are ciliated mechanoreceptive sensory cells responsible for the exquisite sensitivity of the auditory and vestibular systems. In the auditory system, these cells are immersed in endolymph with a relatively high K^+ concentration and positive potential, which establishes a strong electrochemical gradient favoring K^+ influx into the cells (1–3). Sound propagating through the cochlea generates shearing forces on the apical stereocilia bundle of hair cells. Deflection of the stereocilia opens mechanically gated cation channels [i.e., TMC1/2; (4–6)], which permits K^+ influx into the hair cells [mechanoelectrical transduction (MET) current] and drives membrane depolarization (7, 8). The high K^+ concentration of the endolymph is key to this pathway and is produced by active secretion of K^+ into the endolymph by strial marginal cells via a process that includes K^+ channels and Na^+/K^+ ATPase (9–11).

The hair cells of the inner ear are thought to have evolved from anatomically similar cells found in the lateral line of fishes and amphibians (reviewed by ref. 12). The lateral line system detects the movement of water around the body and is critical for survival, as it mediates behaviors such as predator avoidance, prey capture, and navigation (13–16). Unlike the hair cells of the inner ear, the lateral line hair cells lie on the surface of the body and are typically surrounded by a potentially unstable external environment rather than a regulated, K^+-rich endolymph. Work in amphibians in the 1970s indicated that the gelatinous cupula that partially encapsulates the lateral line hair cells maintains an ionic microenvironment comparable to the inner ear endolymph, which establishes the ionic gradient necessary for cation influx–mediated mechanotransduction (17, 18). It has often been assumed that a similar mechanism is responsible for mechanotransduction in other aquatic organisms, including freshwater fishes.

Although the lateral line of freshwater zebrafish is a powerful model system for understanding hair cell physiology (19–21), this foundational hypothesis has remained largely untested. Here, we show that the ionic microenvironment in the cupula of the superficial neuromasts of zebrafish larvae is indistinguishable from the surrounding freshwater. Electrochemical calculations indicate that the freshwater inhabited by zebrafish does not provide ionic gradients sufficient to support the putative cation-mediated mechanotransduction mechanism. Instead, our results suggest an alternative process driven by anion efflux. For cells in contact with ion-poor extracellular saline, typical negative resting membrane potentials and intracellular Cl^- concentrations are sufficient to generate anion efflux capable of inducing robust membrane depolarization. Although studies of sensory physiology often focus on cation-mediated transduction process, anion efflux has been observed to contribute to signal amplification in vertebrate chemosensory receptors, which often directly interface with an unregulated external environment (22–26). It has also been argued that anion efflux may confer favorable properties, including reduced sensitivity to large variations in extracellular ionic composition (27, 28).

Significance

Hair cells in vertebrates are specialized sensory cells with a central role in hearing, balance, and flow sensing. The process by which hair cells transduce mechanical stimuli has been the subject of intense study, frequently with the implicit assumption that hair cells in different sensory systems and across species employ a similar transduction mechanism. Here, it is shown that the hair cells of the zebrafish lateral line system use a substantially different mechanism driven by the efflux of anions rather than the influx of cations. These results establish a new perspective for examining the physiology and evolution of hair cells and other sensory cells.

[1]E.T.L. and Y.V.B. contributed equally to this work.

[2]To whom correspondence may be addressed. Email: james.strother@whitney.ufl.edu or jliao@whitney.ufl.edu.

Results

The Cupula Does Not Provide a Cation-Rich Microenvironment for Lateral Line Hair Cells. We first examined whether the cupula of the superficial neuromasts contained an elevated K^+ concentration capable of supporting mechanotransduction. Animals were bathed in a freshwater medium (E3 saline) with a K^+ selective fluorescent indicator (IPG-4). Using confocal microscopy, we found that fluorescence in the cupula was nearly indistinguishable from that of the surrounding water, suggesting that the cupula does not maintain elevated K^+ concentrations (Fig. 1 *A* and *B*). To quantify the K^+ concentration within the cupula, the indicator was saturated by adding K^+ to the surrounding medium, and the recorded fluorescence values were fit to a model that incorporates both the binding affinity of the indicator and potential differences in indicator concentration between the cupula and medium. Consistent with our qualitative observations, the calculated K^+ concentration of the cupula was not significantly different from that of the surrounding medium ($P = 0.26$, $N = 11$; Fig. 1*C*). Analogous experiments were then performed examining each of the major cations present in freshwater saline and again no significant differences were found between the cupula and the surrounding water (Na^+: $P = 0.88$, $N = 8$; Ca^{2+}: $P = 0.45$, $N = 9$; H^+: $P = 0.30$, $N = 8$; Fig. 1*D*). We also examined the Cl^- concentration within the cupula, since it is the likely counterion for any cation, and found that it was also not significantly different from the freshwater medium ($P = 0.43$, $N = 6$, Fig. 1*D*). These results indicate that the cupula does not support an ionic microenvironment, and the apical surfaces of the lateral line hair cells are directly exposed to an ion-poor freshwater saline that is markedly different from the endolymph of the inner ear (2, 3, 29–31).

To systematically explore the consequences of the hair cells being exposed to an ion-poor environment, we calculated the membrane reversal potential for a MET channel in different extracellular solutions, assuming relative permeabilities similar to other hair cells (*SI Appendix, Membrane Reversal Potentials*). We found that in a freshwater medium (E3 saline), MET conductance would be expected to produce K^+ efflux and hyperpolarization rather than depolarization, which suggests that K^+ current is not the primary driver of transduction (Fig. 1*E*). MET conductance is only predicted to induce membrane depolarization sufficient to open the voltage-gated Ca^{2+} channels on the basolateral membrane [$Ca_V 1.3$, (32)] in water with cation concentrations much greater than those in the natural habitat of zebrafish [Fig. 1*E*, (29–31)]. Although the chemical gradient favors Ca^{2+} influx into the hair cell, this influx is unable to overcome the hyperpolarizing effect generated by K^+ efflux given the estimated relative permeabilities of the MET channels. Ca^{2+} currents would therefore only be sufficiently depolarizing if the MET channels displayed Ca^{2+} selectivity far in excess of that reported in other systems (4). We next calculated the reversal potential for a hypothetical Cl^- channel and found that Cl^- conductance would be expected to readily drive Cl^- efflux from the hair cells and membrane depolarization in a wide range of external environments (Fig. 1*E*). In total, these results argue against K^+ influx as a mechanism for lateral line hair cell depolarization and suggest that Ca^{2+} influx or Cl^- efflux may have more central roles.

The lack of an ionic microenvironment in the cupula would profoundly affect the mechanotransduction mechanisms available to hair cells. We next conducted a series of experiments and simulations further exploring whether the physical properties of the cupula could support such a microenvironment. We first examined the diffusion of charged molecules within the cupula by rapidly introducing a negatively charged small molecule fluorophore
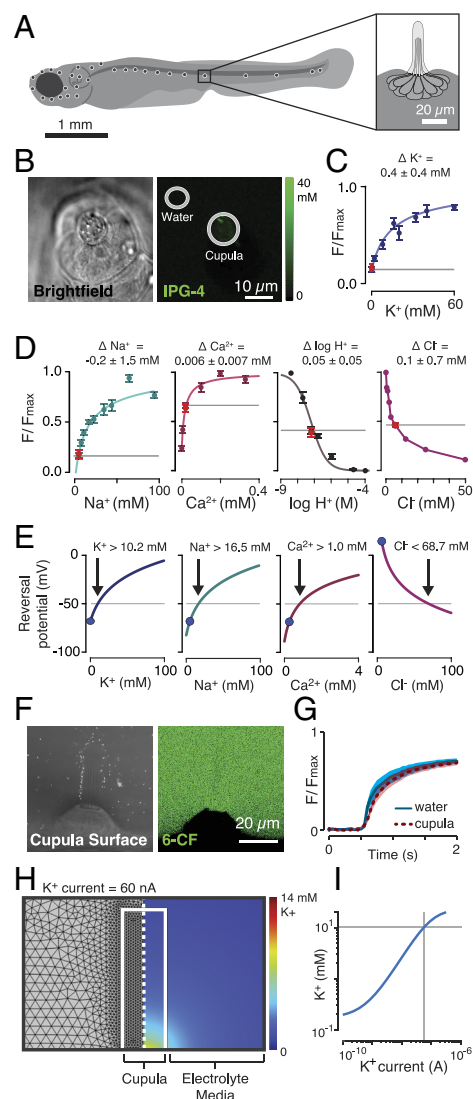

Fig. 1. The ionic microenvironment of the cupula resembles freshwater and cannot support cation influx–mediated depolarization. (*A*) Superficial neuromasts of the lateral line system in larval zebrafish. (*B*) In vivo visualization of K^+ in the vicinity of a neuromast using the fluorescent probe IPG-4 (*Left*: brightfield; *Right*: IPG-4). (*C*) Fluorescence of K^+ probe in solutions with varying K^+ concentrations (blue, error bars are ± SEM, curve is fit model), fluorescence expected for an environment matching the surrounding freshwater medium (E3 saline; horizontal gray line), and measured fluorescence within the cupula (red dot, error bars are ± SEM, error bars are small and may be partially obscured). The similarity of the cupula fluorescence (red dot) and freshwater medium fluorescence (gray line) suggests the K^+ concentration in the cupula is similar to the surrounding medium. Using these measured values, the difference between the K^+ concentration in the cupula and the surrounding medium was also calculated (ΔK^+, mean ± SEM). (*D*) Results from experiments similar to (*C*) except examining Na^+ (probe: ING-2), Ca^{2+} (probe: Fluo-5 N), H^+ (probe: BCECF), and Cl^- (probe: MQAE). In all cases, ion concentrations within the cupula matched those of the surrounding medium. (*E*) Predicted reversal potentials for MET channels as a function of cupula cation concentration. The estimated opening potential of voltage-gated Ca^{2+} channels at the basal membrane is indicated (−50 mV, horizontal line). The cation concentration necessary to reach this potential (black arrow) and the concentration in a freshwater medium (blue dot) are also indicated. The predicted reversal potential for a hypothetical chloride channel is also shown (right). (*F*) Images showing penetration of a charged fluorophore (6-carboxyfluorescein, 6-CF) into neuromast cupula (*Left*: cupula surface visualized with microspheres, *Right*: 6-CF). (*G*) From the same experiments as (*F*), time series showing rapid increase in fluorescence in both the medium around the cupula and within the cupula after introduction of the charged fluorophore. (*H*) Simulation of a hypothetical K^+ microenvironment, produced by solving 3D Nernst-Plank equations (*Left*: mesh, right: K^+ distribution for K^+ current = 60nA). (*I*) K^+ concentration at apical surface of hair cells as a function of K^+ secretion current [horizontal gray line: estimated K^+ concentration necessary for depolarization (10.2 mM), vertical gray line: corresponding K^+ efflux current (56 nA)].

(6-carboxyfluorescein; 6-CF) around the cupula and imaging its diffusion from the medium into the cupula (Fig. 1*F*). There were no significant differences between the rate at which fluorescence increased in the cupula and the surrounding water, suggesting that charged molecules rapidly penetrate the cupula [relative time constant = 0.88 ± 0.06 (mean ± SEM), $P = 0.076$, N = 9, Fig. 1*G*]. Computational simulations confirmed that this experimental setup had sufficient resolution to detect meaningful differences in the diffusive properties of the cupular matrix (*SI Appendix*, Fig. S1 *A–C*). This finding is also consistent with empirical studies of the ultrastructure of lateral line cupulae, which identified no membrane or other dense surface structure (33, 34).

We next evaluated the ion currents that would be necessary to sustain a K^+ reservoir in the cupula using computational simulations. Since this configuration violates the assumptions of a typical neuron electrical equivalent circuit (35), we simulated these dynamics by directly solving the full three-dimensional Nernst–Planck equations using the finite element method (Fig. 1*H*). Based on the above diffusion experiments, we estimated the diffusion coefficients for ions moving through the cupular matrix to be similar to that of water and assumed a constant rate of K^+ secretion into the matrix at the base of the neuromast. We found that a K^+ current of 56 nA would be needed to produce the K^+ concentration of 10.2 mM required for depolarizing MET conductance (Fig. 1 *E* and *I*). Although the ionoregulatory currents of the neuromast have not been quantified, these K^+ current values are several orders of magnitude greater than the resting MET current of hair cells (36, 37). These results indicate that recently described skin-derived ionocytes are unlikely to maintain a K^+ microenvironment at the apical surface of the hair cells but may instead support regulation of the extracellular environment at the basolateral surfaces (38).

Cumulatively, these experiments indicate that the cupula does not maintain a cation-rich microenvironment sufficient to support hair cell depolarization, challenging a long-standing assumption that hair cell transduction is cation driven in the lateral line system of zebrafish and other freshwater fishes.

Lateral Line Function Only Requires Micromolar Extracellular Calcium. What other mechanisms could mediate hair cell depolarization? We next tested the hypothesis that Ca^{2+} could contribute to hair cell depolarization, given its reversal potential and assuming MET channels with unusually high Ca^{2+} selectivity. Hair cells expressing the fluorescent calcium indicator GCaMP6s were imaged while mechanically deflecting the cupula with a piezoelectric transducer (Fig. 2*A*). Changes in fluorescence near the basal surface of the hair cells were observed, which have been attributed to Ca^{2+} influx through voltage-gated channels on the basal membrane (21). Hair cells produced robust responses to this stimulus in a freshwater medium (E3 saline, 330 μM Ca^{2+}; $P < 0.001$, df = 27; Fig. 2*A*). Interestingly, we found that hair cells continue to respond in a medium with substantially reduced Ca^{2+} concentrations (20 μM Ca^{2+}; $P = 0.04$, df = 3; Fig. 2*A*) and that these responses were indistinguishable from those observed in freshwater saline ($P = 0.13$, df = 3). The insensitivity of hair cell responses to the extracellular Ca^{2+} concentration may suggest that Ca^{2+} current is not crucial for mechanotransduction. However, responses in 0 μM Ca^{2+} medium were significantly reduced compared to those in freshwater saline ($P = 0.02$, df = 9; Fig. 2*A*). This indicates that environmental Ca^{2+} modulates MET currents in naturalistic freshwater media, consistent with observations in zebrafish and other species (8, 39–43).

To further examine the role of Ca^{2+} currents in hair cell depolarization, we used the Nernst–Planck computational model to
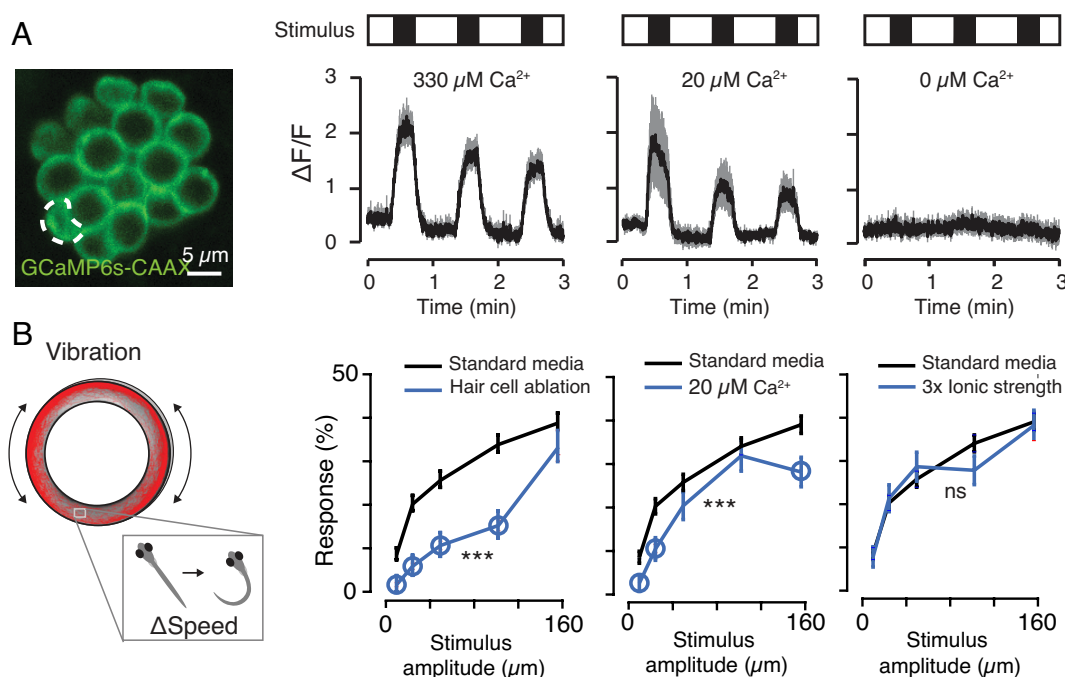

Fig. 2. Only micromolar extracellular calcium is required for lateral line function. (*A*) Response of hair cells to a mechanical stimulus, recorded by imaging genetically expressed fluorescent calcium indicator GCaMP6s-CAAX at the basal membrane (*Left*: typical image, region of interest indicated; *Right*: responses in 330 μM, 20 μM, and 0 μM Ca^{2+}, mean ± SEM). Hair cell responses in micromolar Ca^{2+} medium are comparable to those in a freshwater medium (E3 saline), while responses are abolished in a calcium-free medium. (*B*) Behavioral response of zebrafish larvae to a mechanical stimulus under varying conditions, recorded with a unique behavioral assay that employs an oscillatory Couette cell to produce a pure-shear flow stimulus (*Left*: schematic of behavioral setup with typical trajectory in red; *Right*: probability of response following neomycin-induced hair cell ablation, in 20 μM Ca^{2+} medium, and in 3× ionic strength medium). Asterisks indicate statistically significant differences integrated across stimulus intensities (*$P < 0.05$, **$P < 0.01$, ***$P < 0.001$), open circles represent significant pairwise comparisons ($P < 0.05$), and results are shown as mean ± SEM.

estimate the maximum sustainable Ca^{2+} current in the reduced Ca^{2+} medium (20 μM). We simulated a scenario where the stereocilia tips have infinite Ca^{2+} conductance, and the total Ca^{2+} current is limited by the diffusion of Ca^{2+} through the surrounding medium (*SI Appendix*, Fig. S1*D*). Using this approach, the maximum Ca^{2+} current into an isolated hair cell was estimated to be 2.8 pA, which is orders of magnitude smaller than a typical MET current (36, 37). These results indicate that the reduced Ca^{2+} medium cannot support large Ca^{2+} currents and provides further evidence that Ca^{2+} current is not critical to mechanotransduction. These findings do not rule out that possibility that Ca^{2+} current contributes to mechanotransduction in media with higher Ca^{2+} concentrations.

We next examined whether these cellular-scale differences were reciprocated at the organismal level by recording the effects of low Ca^{2+} environments on the behavior of freely swimming larvae. A number of behavioral assays have been successfully employed for assessing lateral line function in zebrafish larvae, including assays measuring C-start escapes in response to impulsive stimuli and assays measuring rheotactic responses (13–15). However, the contribution of multiple sensory modalities (e.g., vestibular, acoustic, visual) to behavioral responses often presents a challenge when developing such assays. Since the superficial lateral line is principally sensitive to shear at the body surface (44), we designed a novel behavioral assay that uses an oscillatory Couette cell to produce a shearing flow without accompanying pressure waves (*SI Appendix*, Fig. S2). The position and swimming speed of animals were continuously monitored, and stimuli of varying intensities were presented at random intervals. Each stimulus that produced a significant change in swimming speed (outside 95% CI) was recorded and then the net response probability was calculated as a function of stimulus intensity. In order to reduce both habituation and activation of collateral sensory modalities, we intentionally examined small stimulus intensities that produced modest changes in behavior with relatively low response probabilities rather than escape responses with high probability.

To evaluate the efficacy of this assay, we confirmed that animals responded in an intensity-dependent manner and that neomycin-induced hair cell ablation dramatically decreased this response (Fig. 2*B*). Next, we examined how low environmental Ca^{2+} affects lateral line sensitivity and found that animals displayed reduced but robust responses even with Ca^{2+} decreased by >15× (21% decrease with 50 μm stimulus, omnibus $P < 0.001$, N = 30 exp/94 ctrl). These results are consistent with our imaging data and data from other species (39, 45). Using this same assay, we then examined how lateral line sensitivity is altered by increases in the ionic strength of the freshwater environment. The responses of animals in a medium with a 3× increase in ionic strength were not significantly different from those in a freshwater medium (E3 saline, omnibus $P > 0.05$, N = 30 exp/94 ctrl). Media with higher ion concentrations were also explored, and significant decreases in sensitivity were detected, but such ion concentrations far exceed the values observed in the natural habitat of zebrafish and these effects may result from osmotic stress rather than a specific interaction with the lateral line (*SI Appendix*, Fig. S3). In total, these findings suggest that extracellular Ca^{2+} modulates the mechanotransduction process but does not provide the primary ion current driving hair cell depolarization.

Calcium-Activated Anion Efflux Contributes to Hair Cell Depolarization. Since the electrochemical gradient between hair cells and freshwater strongly favors anion efflux, we next examined whether this efflux could be contributing to mechanotransduction. We began by leveraging available transcriptome data to generate testable hypotheses. We analyzed published transcriptome scRNA-seq data collected from zebrafish lateral line neuromasts (46) for cells that expressed a hair

cell marker (tmc2b), filtered transcripts for genes associated with ion channel activity, and then reviewed the resulting list for genes with anion efflux activity. This analysis indicated that the lateral line hair cells may express the calcium-activated anion channel Anoctamin-2b (ANO2b), also known as TMEM16b (Fig. 3*A*).
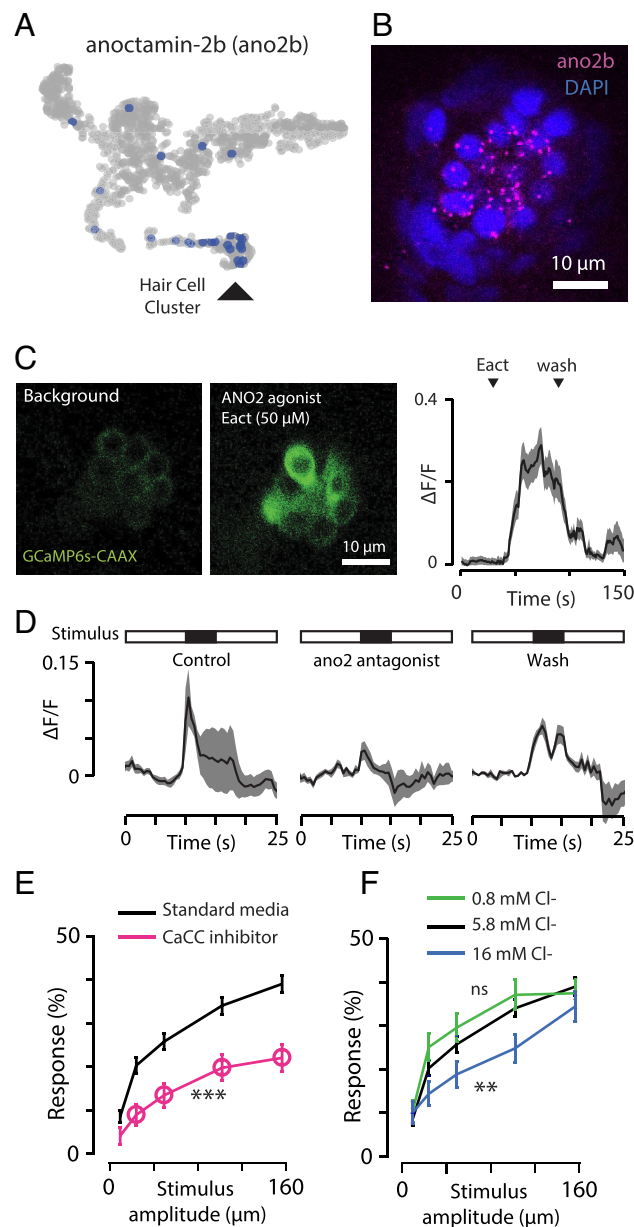

Fig. 3. Calcium-activated chloride channels are expressed in lateral line hair cells, sufficient to activate hair cells, and necessary for functional responses at the cellular and organismal level. (*A*) Visualization of single-cell transcriptome data for lateral line neuromast showing expression of anoctamin-2b (*ano2b*) in the hair cell cluster [t-SNE plot, data from (47)]. (*B*) In situ hybridization image showing *ano2b* expression in a lateral line neuromast (punctate pattern consistent with single-molecule RNA-FISH). (*C*) Response of hair cells to the Ano2 agonist Eact, recorded at the basal membrane using a genetically expressed fluorescent calcium indicator (*Left* and *Middle*: typical images, right: measured ΔF/F for introduction and washout, mean ± SEM). (*D*) Response of hair cells to cupula deflection while bathed in standard saline (control; *Left*), an Ano2 antagonist (25 μM T16Ainh; *Middle*), and after washout (*Right*; mean ± SEM). (*E*) Effect of the calcium-activated chloride channel (CaCC) inhibitor NFA on the behavioral response of zebrafish larvae to a mechanical stimulus. Asterisks indicate statistically significant differences integrated across stimulus intensities (*$P < 0.05$, **$P < 0.01$, ***$P < 0.001$), open circles represent significant pairwise comparisons ($P < 0.05$), and results are shown as mean ± SEM. (*F*) Similar to (*E*), except showing the effect of decreasing the electrochemical gradient supporting chloride efflux by increasing extracellular chloride.

To verify this expression, *ano2b* transcripts were labeled using HCR RNA-FISH. We observed *ano2b* labeling in lateral line hair cells, olfactory epithelium, and the dorsal habenula (Fig. 3*B* and SI Appendix, Fig. S4). The expression of anoctamin in the olfactory epithelium is consistent with similar findings in mammalian olfactory epithelium (47), and *ano2b* expression in the dorsal habenula of zebrafish has been previously reported (48).

We next examined whether calcium-activated chloride channels are capable of inducing depolarization of the lateral line hair cells. Using zebrafish larvae that express a fluorescent calcium indicator in hair cells [*myo6b:GCaMP6s-CAAX*; (21)], we recorded hair cell responses to the Anoctamin2 agonist Eact (49). This agonist induced immediate and robust increases in intracellular calcium at the basolateral membrane ($P < 0.001$, df = 58), which were reversible upon washout (Fig. 3*C*). We then recorded hair cell responses to mechanical stimulation in the presence of the Anoctamin2 antagonist T16A$_{inh}$-A01 (50). We found that this blockade produced significant reductions ($P = 0.026$, df = 24) of hair cell responses to mechanical stimuli that recovered after a washout ($P = 0.017$, df = 17; Fig. 3*D*). These responses are consistent with the hypothesis that calcium-activated anion channels contribute to mechanotransduction in the lateral line hair cells.

We then sought to determine whether these effects were reflected in the responses of an intact, behaving animal. When we examined the behavioral response of animals that had been treated with the calcium-activated chloride channel blocker niflumic acid (NFA) (51), we found that they exhibited a marked decrease in behavioral responses relative to untreated animals (48% decrease with 50 μm stimulus, omnibus $P < 0.001$, N = 30 exp/94 ctrl, Fig. 3*E*). Although interpretations of behavioral data must allow for the possibility of nonspecific effects, these results are consistent with the notion that calcium-activated Cl⁻ conductance supports lateral line function. We also examined the sensitivity of animals in media in which Cl⁻ concentrations were varied to manipulate the strength of the electrochemical gradient supporting anion efflux. We found that increasing this electrochemical gradient by reducing extracellular Cl⁻ (0.8 mM) produced a small increase in the response to stimuli relative to a freshwater medium (5.2 mM), although this effect was not significant (omnibus $P > 0.05$, N = 30 exp/94 ctrl, Fig. 3*F*). Conversely, we found that decreasing this gradient by increasing extracellular Cl⁻ (16 mM) reduced the response (27% decrease with 50 μm stimulus, omnibus $P < 0.01$, N = 30 exp/94 ctrl, Fig. 3*F*) relative to a freshwater medium. This suppression, but not termination, of lateral line sensitivity is consistent with the reversal potential still favoring anion efflux at this extracellular Cl⁻ concentration (Fig. 1*E*). Higher Cl⁻ concentrations were examined, and similar results were observed (SI Appendix, Fig. S3), although such salines impose a stronger osmotic stress that may complicate interpretation. Cumulatively, these results provide further support for the role of anion efflux in lateral line mechanotransduction.

A Hypothesis for Lateral Line Mechanotransduction. The MET channels in hair cells are permeable to both monovalent (K⁺, Na⁺) and divalent (Ca²⁺) cations (7, 8). It has long been speculated that mechanotransduction in lateral line hair cells was mediated by cation influx through the apical membrane, similar to the inner ear. Here, we present evidence that the depolarization of lateral line hair cells is instead supported by anion efflux rather than cation influx. Although further work is required to fully establish the complete mechanotransduction pathway, our results suggest a new hypothesis: deflection of the hair cell bundle opens MET channels allowing influx of trace amounts of Ca²⁺, which interacts with Ca²⁺-activated Cl⁻ channels, leading to Cl⁻ efflux through the
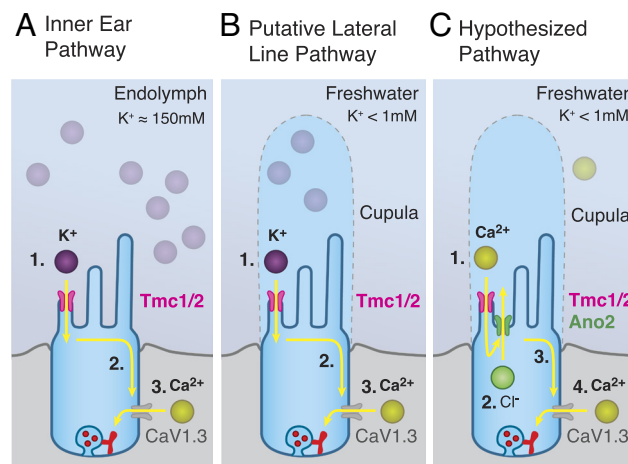

Fig. 4. Calcium-activated chloride channels amplify hair cell signaling in environments of low ionic strength. (*A*) Established inner ear pathway: Inner ear hair cells are bathed in a K⁺-rich endolymph. 1. As the stereocilia deflect, mechano-electrical transduction (MET) channels open, allowing K⁺ influx into the hair cells. 2. Cation influx initiates membrane depolarization. 3. Voltage-gated calcium channels allow Ca²⁺ influx at the basolateral membrane and subsequent vesicle fusion. (*B*) Putative lateral line pathway: Similar to (*A*), except the cupula encapsulating the lateral line hair cells maintains an ionic microenvironment that supports K⁺ influx. (*C*) Hypothesized pathway: The apical membrane of the lateral line hair cells in zebrafish is exposed to external freshwater environments with insufficient cations to directly drive depolarization. We hypothesize that depolarization is mediated by anion efflux through the following processes: 1. Trace amounts of Ca²⁺ influx through MET channels. 2. Calcium-activated chloride channels open. 3. Cl⁻ efflux initiates membrane depolarization. 4. Voltage-gated calcium channels support vesicle fusion.

apical membrane that induces membrane depolarization (Fig. 4). Several lines of evidence support this hypothesis, including 1) the electrochemical gradient across the apical membrane is unable to support cation influx induced depolarization, 2) hair cells only require micromolar extracellular Ca²⁺ to function, 3) the hair cells express Ca²⁺-activated Cl⁻ channels, 4) activating these channels induces hair cell depolarization, and 5) blocking these channels reduces the response of animals and individual hair cells to mechanosensory stimuli. This hypothesis raises many interesting new questions. It is unclear what the relative contributions of *ano2b* and other anion channels are to mechanotransduction or how the relative ion permeabilities of zebrafish lateral line MET channels affect Ca²⁺ influx and potential K⁺ efflux. It is unknown how Ca²⁺ compartmentalization and basal/apical differences in Ca²⁺ concentration influence hair cell function. Future studies exploring these questions are likely to yield novel and general insights into the physiology of mechanotransduction.

Discussion

Anion efflux–mediated sensory transduction provides several potential advantages for cells exposed to ion-poor environments (28). Anion efflux is expected to be robust to fluctuating external conditions, since the intracellular environment provides a well-regulated source of anions (52) and there is a strong electrochemical gradient supporting efflux across a wide range of external conditions. This intrinsic robustness could allow animals to maintain sensitivity in dynamic environments, without the need for secondary pathways for modulation or auxiliary structures that maintain a stable extracellular microenvironment. Although transduction mechanisms leveraging anion efflux have received much less attention than pathways utilizing cation influx, signal amplification through anion efflux provides an elegant solution to the challenge of fluctuating dynamic environments. This mechanism has also been found in

vertebrate olfactory receptor neurons (22–26). There, odorant receptors act via a G-protein-coupled cascade to increase cAMP, which induces opening of cyclic nucleotide-gated cation channels. This leads to an influx of Ca^{2+} and subsequent opening of Ca^{2+}-activated Cl^- channels (Ano2). This striking similarity between mechanoreceptive and olfactory systems, two apparently disparate sensory modalities, may suggest convergent evolution in systems exposed to dynamic extracorporeal environments.

The lateral line appears to have evolved in early vertebrates (12), but it is not clear whether these early vertebrates occupied marine or freshwater environments, or both at different life stages (53, 54). In a marine environment, high Na^+ and Cl^- concentrations at the apical surface would easily support cation influx–mediated depolarization and make Cl^- conductance hyperpolarizing. Here, we show that in freshwater environments, transduction would require either the establishment of an ionic microenvironment that can support cation influx or a mechanism based on anion efflux. As a result, migrations between marine and freshwater environments would be expected to have dramatic effects on lateral line function, and yet these migrations are routine for catadromous, anadromous, and euryhaline fishes. Prior studies have found that freshwater amphibians generate a K^+ microenvironment within the cupula (17, 18), while our results suggest that zebrafish larvae employ anion efflux. Understanding the evolutionary origins of lateral line hair cells and how these systems evolved as fishes and related animals entered new environments would provide important insights into hair cell physiology and the evolution of sensory systems.

The vertebrate lateral line system continues to serve as a powerful model for dissecting the basic principles of hearing and balance. However, prior studies by our labs and others have typically examined lateral line physiology in ion-rich extracellular saline that mimics vertebrate blood rather than the ion-poor saline these animals naturally inhabit (37, 55). The use of cation-rich saline would be expected to introduce an artificial cation influx while masking naturally occurring anion efflux. As such, this work highlights the necessity of studying sensory systems in the context in which they evolved in order to decipher their true properties and capacities.

Materials and Methods

Detailed methods are provided in the *SI Appendix*. Briefly, the ionic composition of the neuromast cupula was measured using ion indicators (IPG-4, ING-2, Fluo5N, BCECF, and MQAE). The sensitivity and responses to pharmacological agents of the hair cells were determined using genetically expressed fluorescent calcium indicators (myo6b:GCaMP6s-CAAX). Lastly, effects on the behavioral responses of the animals to mechanical stimuli were measured using a unique behavioral assay based on a shear-only flow stimulus.

Data, Materials, and Software Availability. All study data are included in the article and/or *SI Appendix*. The code and scripts used for analysis are available from public repositories (Neuron Image Analysis toolkit: https://bitbucket.org/jastrother/neuron_image_analysis (56), and Larval Proving Grounds toolkit: https://bitbucket.org/jastrother/larval_proving_grounds) (57).

1. R. Fettiplace, Hair cell transduction, tuning, and synaptic transmission in the mammalian cochlea. *Compr. Physiol.* **7**, 1197–1227 (2011).
2. S. K. Bosher, R. L. Warren, Very low calcium content of cochlear endolymph, an extracellular fluid. *Nature* **273**, 377–378 (1978).
3. C. A. Smith, O. H. Lowry, M.-L. Wu, The electrolytes of the labyrinthine fluids. *Laryngoscope* **64**, 141–153 (1954).
4. B. Pan *et al.*, TMC1 and TMC2 are components of the mechanotransduction channel in hair cells of the mammalian inner ear. *Neuron* **79**, 504–515 (2013).
5. B. Pan *et al.*, TMC1 forms the pore of mechanosensory transduction channels in vertebrate inner ear hair cells. *Neuron* **99**, 736–753.e6 (2018).
6. Y. Jia *et al.*, TMC1 and TMC2 proteins are pore-forming subunits of mechanosensitive ion channels. *Neuron* **105**, 310–321.e3 (2020).
7. D. P. Corey, A. J. Hudspeth, Ionic basis of the receptor potential in a vertebrate hair cell. *Nature* **281**, 675–677 (1979).
8. H. Ohmori, Mechano-electrical transduction currents in isolated vestibular hair cells of the chick. *J. Physiol.* **359**, 189–217 (1985).
9. M. J. Dixon *et al.*, Mutation of the Na-K-Cl co-transporter gene Slc12a2 results in deafness in mice. *Hum. Mol. Genet.* **8**, 1579–1584 (1999).
10. D. C. Marcus, T. Wu, P. Wangemann, P. Kofuji, KCNJ10 (Kir4. 1) potassium channel knockout abolishes endocochlear potential. *Am. J. Physiol. Cell Physiol.* **282**, C403–C407 (2002).
11. P. Wangemann, J. Liu, D. C. Marcus, Ion transport mechanisms responsible for K+ secretion and the transepithelial voltage across marginal cells of stria vascularis in vitro. *Hearing Res.* **84**, 19–29 (1995).
12. J. M. Jørgensen, "Evolution of the octavolateralis sensory cells" in *The Mechanosensory Lateral Line*, S. Coombs, P. Görner, H. Münz, Eds. (Springer, 1989), pp. 115–145.
13. M. J. McHenry, K. E. Feitl, J. A. Strother, W. J. Van Trump, Larval zebrafish rapidly sense the water flow of a predator's strike. *Biol. Lett.* **5**, 477–479 (2009).
14. P. J. Mekdara, M. A. B. Schwalbe, L. L. Coughlin, E. D. Tytell, The effects of lateral line ablation and regeneration in schooling giant danios. *J. Exp. Biol.* **221**, jeb175166 (2018).
15. J. Olszewski, M. Haehnel, M. Taguchi, J. C. Liao, Zebrafish larvae exhibit rheotaxis and can escape a continuous suction source using their lateral line. *PLoS One* **7**, e36661 (2012).
16. A. Suli, G. M. Watson, E. W. Rubel, D. W. Raible, Rheotaxis in larval zebrafish is mediated by lateral line mechanosensory hair cells. *PLoS One* **7**, e29727 (2012).
17. F. P. McGlone, I. J. Russell, O. Sand, Measurement of calcium ion concentrations in the lateral line cupulae of Xenopus laevis. *J. Exp. Biol.* **83**, 123–130 (1979).
18. I. J. Russell, P. M. Sellick, Measurement of potassium and chloride ion concentrations in the cupulae of the lateral lines of Xenopus laevis. *J. Physiol.* **257**, 245–255 (1976).
19. T. Nicolson *et al.*, Genetic analysis of vertebrate sensory hair cell mechanosensation: The zebrafish circler mutants. *Neuron* **20**, 271–283 (1998).
20. A. J. Ricci *et al.*, Patch-clamp recordings from lateral line neuromast hair cells of the living zebrafish. *J. Neurosci.* **33**, 3131–3134 (2013).
21. Q. Zhang *et al.*, Synaptically silent sensory hair cells in zebrafish are recruited after damage. *Nat. Commun.* **9**, 1–16 (2018).
22. A. B. Stephan *et al.*, ANO2 is the cilial calcium-activated chloride channel that may mediate olfactory amplification. *Proc. Natl. Acad. Sci. U.S.A.* **106**, 11776–11781 (2009).
23. S. J. Kleene, R. C. Gesteland, Calcium-activated chloride conductance in frog olfactory cilia. *J. Neurosci.* **11**, 3624–3629 (1991).
24. G. Lowe, G. H. Gold, Nonlinear amplification by calcium-dependent chloride channels in olfactory receptor cells. *Nature* **366**, 283–286 (1993).
25. A. P. Cherkashin *et al.*, Expression of calcium-activated chloride channels Ano1 and Ano2 in mouse taste cells. *Pflugers Arch – Eur. J. Physiol.* **468**, 305–319 (2016).
26. J. Reisert, J. Lai, K.-W. Yau, J. Bradley, Mechanism of the excitatory Cl- response in mouse olfactory receptor neurons. *Neuron* **45**, 553–561 (2005).
27. T. Kurahashi, K.-W. Yau, Olfactory transduction: Tale of an unusual chloride current. *Curr. Biol.* **4**, 256–258 (1994).
28. J. Reisert, J. Reingruber, Ca2+-activated Cl- current ensures robust and reliable signal amplification in vertebrate olfactory receptor neurons. *Proc. Natl. Acad. Sci. U.S.A.* **116**, 1053–1058 (2019).
29. R. Spence, G. Gerlach, C. Lawrence, C. Smith, The behaviour and ecology of the zebrafish, Danio rerio. *Biol. Rev.* **83**, 13–34 (2008).
30. R. Spence *et al.*, The distribution and habitat preferences of the zebrafish in Bangladesh. *J. Fish Biol.* **69**, 1435–1448 (2006).
31. M. M. Sarin, S. Krishnaswami, Major ion chemistry of the Ganga-Brahmaputra river systems, India. *Nature* **312**, 538–541 (1984).
32. A. Brandt, D. Khimich, T. Moser, Few CaV1.3 channels regulate the exocytosis of a synaptic vesicle at the hair cell ribbon synapse. *J. Neurosci.* **25**, 11577–11585 (2005).
33. B. S. Dezfuli, S. Magosso, E. Simoni, K. Hills, R. Berti, Ultrastructure and distribution of superficial neuromasts of blind cavefish, Phreatichthys andruzzii, juveniles. *Microscopy Res. Technique* **72**, 665–671 (2009).
34. Å. Flock, J. M. Jørgensen, The ultrastructure of lateral line sense organs in the juvenile salamander Ambystoma mexicanum. *Cell Tissue Res.* **152**, 283–292 (1974).
35. A. L. Hodgkin, A. F. Huxley, A quantitative description of membrane current and its application to conduction and excitation in nerve. *J. Physiol.* **117**, 500–544 (1952).
36. M. Beurg, J.-H. Nam, A. Crawford, R. Fettiplace, The actions of calcium on hair bundle mechanics in mammalian cochlear hair cells. *Biophys. J.* **94**, 2639–2653 (2008).
37. J. Olt, S. L. Johnson, W. Marcotti, In vivo and in vitro biophysical properties of hair cells from the lateral line and inner ear of developing and adult zebrafish. *J. Physiol.* **592**, 2041–2058 (2014).
38. J. Peloggia *et al.*, Adaptive cell invasion maintains lateral line organ homeostasis in response to environmental changes. *Dev. Cell* **56**, 1296–1312 (2021).
39. O. Sand, Effects of different ionic environments on the mechano-sensitivity of lateral line organs in the mudpuppy. *J. Comp. Physiol.* **102**, 27–42 (1975).
40. A. B. Coffin, K. E. Reinhart, K. N. Owens, D. W. Raible, E. W. Rubel, Extracellular divalent cations modulate aminoglycoside-induced hair cell death in the zebrafish lateral line. *Hearing Res.* **253**, 42–51 (2009).
41. M. Beurg, M. G. Evans, C. M. Hackney, R. Fettiplace, A large-conductance calcium-selective mechanotransducer channel in mammalian cochlear hair cells. *J. Neurosci.* **26**, 10992–11000 (2006).

42. V. Di Donato, T. O. Auer, K. Duroure, F. Del Bene, Characterization of the calcium binding protein family in zebrafish. *PLoS One* **8**, e53299 (2013).

43. A. J. Ricci, A. C. Crawford, R. Fettiplace, Tonotopic variation in the conductance of the hair cell mechanotransducer channel. *Neuron* **40**, 983–990 (2003).

44. M. J. McHenry, J. A. Strother, S. M. Van Netten, Mechanical filtering by the boundary layer and fluid–structure interaction in the superficial neuromast of the fish lateral line system. *J. Comp. Physiol. A* **194**, 795 (2008).

45. H. E. Karlsen, O. Sand, Selective and reversible blocking of the lateral line in freshwater fish. *J. Exp. Biol.* **133**, 249–262 (1987).

46. M. E. Lush *et al.*, scRNA-Seq reveals distinct stem cell populations that drive hair cell regeneration after loss of Fgf and Notch signaling. *Elife* **8**, e44431 (2019).

47. S. Rasche *et al.*, Tmem16b is specifically expressed in the cilia of olfactory sensory neurons. *Chem. Senses* **35**, 239–245 (2010).

48. T. N. deCarvalho *et al.*, Neurotransmitter map of the asymmetric dorsal habenular nuclei of zebrafish. *Genesis* **52**, 636–655 (2014).

49. W. Namkung, Z. Yao, W. E. Finkbeiner, A. S. Verkman, Small-molecule activators of TMEM16A, a calcium-activated chloride channel, stimulate epithelial chloride secretion and intestinal contraction. *FASEB J.* **25**, 4048–4062 (2011).

50. W. Namkung, P.-W. Phuan, A. S. Verkman, TMEM16A inhibitors reveal TMEM16A as a minor component of calcium-activated chloride channel conductance in airway and intestinal epithelial cells*. *J. Biol. Chem.* **286**, 2365–2374 (2011).

51. S. Pifferi, M. Dibattista, A. Menini, TMEM16B induces chloride currents activated by calcium in mammalian cells. *Pflügers Archiv-Eur. J. Physiol.* **458**, 1023–1038 (2009).

52. K. Kaila, T. J. Price, J. A. Payne, M. Puskarjov, J. Voipio, Cation-chloride cotransporters in neuronal development, plasticity and disease. *Nat. Rev. Neurosci.* **15**, 637–654 (2014).

53. R. W. Griffith, Freshwater or marine origin of the vertebrates? *Comp. Biochem. Physiol. Part A Physiol.* **87**, 523–531 (1987).

54. L. B. Halstead, W. G. Chaloner, J. D. Lawson, The vertebrate invasion of fresh water. *Philos. Trans. R. Soc. London B Biol. Sci.* **309**, 243–258 (1985).

55. E. T. Lunsford, D. A. Skandalis, J. C. Liao, Efferent modulation of spontaneous lateral line activity during and after zebrafish motor commands. *J. Neurophysiol.* **122**, 2438–2448 (2019).

56. J. A. Strother, Neuron Image Analysis Toolkit. Bitbucket.org. https://bitbucket.org/jastrother/neuron_image_analysis/. Deposited 20 April 2022.

57. J. A. Strother, Larval Proving Grounds Toolkit. Bitbucket.org. https://bitbucket.org/jastrother/larval_proving_grounds/. Deposited 12 May 2023.

Supporting Information for

Anion efflux mediates transduction in the hair cells of the zebrafish lateral line

Elias T. Lunsford, Yuriy V. Bobkov, Brandon C. Ray, James C. Liao, James A. Strother

Corresponding authors: J.A. Strother and J.C. Liao
Email: james.strother@whitney.ufl.edu and jliao@whitney.ufl.edu

This PDF file includes:

Supporting information text
Figures S1 to S5
SI References

Supporting Information Text

Materials and Methods

Animals
Experiments were performed on 4-7 day post fertilization (dpf) zebrafish larvae (*Danio rerio,* AB strain), which were raised in bicarbonate-buffered E3 medium (5 mM NaCl, 0.17 mM KCl, 0.33 mM $CaCl_2$, 0.33 mM $MgSO_4$, 0.35 $NaHCO_3$, 0.27 µM methylene blue, pH 7.2-7.4; modified from (1)) under standard conditions (28°C, 14:10 light:dark) and provided micropowder feed starting at 5 dpf (Microgemma 75, Skretting). All protocols were approved by the University of Florida Institutional Animal Care and Use Committee (Protocols 201910912 & 202200000056).

Cupula ionic composition experiments
Larvae were immobilized by immersion in a paralytic that specifically blocks nicotinic acetylcholine receptors present at the neuromuscular junction (20 µL of 1 mg/mL α-bungarotoxin [Sigma Aldrich] in HEPES-buffered E3 [5 mM NaCl, 0.17 mM KCl, 0.33 mM $CaCl_2$, 0.33 mM $MgSO_4$, 1 mM HEPES, titrated to pH 7.2-7.4]) (2). Larvae were transferred to a coverslip-bottomed recording dish at room temperature (20-22°C), pinned onto a small silicone elastomer pad (5 mm x 1 mm x 1 mm, Sylgard 184) using etched tungsten pins (<50 µm diameter) through the notochord, and then this pad was turned over and pinned to a larger block of silicone elastomer such that the lateral side of the animal faced downward. This lateral-side down configuration enabled imaging of the cupula cross-section for predominantly trunk neuromasts on an inverted confocal microscope. Blood flow was taken as a measure of animal health and only trials with robust blood flow at the beginning and end of the experiment were analyzed. The K^+ concentration within the cupula was measured by perfusing on medium containing the potassium-selective fluorescent indicator (10 µM IPG-4 in HEPES-buffered E3; ION Biosciences), and recording the fluorescence in the cupula and the surrounding medium near the stereocilia (Leica TCS SP5 II, HCX PL APO CS 63x/1.2 water objective, 1 frame/sec, excitation: 514 nm, emission: 530 - 574 nm). Measurements were also made 5 µm and 10 µm above the stereocilia and yielded similar results. Fluorescence values were averaged over a manually selected region-of-interest in ImageJ (v1.48; U. S. National Institutes of Health).

The recorded indicator fluorescence inside of the cupula was not substantially different from the low indicator fluorescence present in the surrounding medium, suggesting that the K^+ concentration in the cupula was similar to that of the surrounding medium. To ensure that this was not a result of low indicator penetration into the cupula or other issues with fluorescence detection, the relationship between K^+ concentration and indicator fluorescence was then measured *in situ*. The K^+ concentration of the medium was incrementally increased by washing in medium with increased KCl (0.2-60 mM total conc.), and changes in the fluorescence within the surrounding medium and cupula were recorded. Again, indicator fluorescence inside of the cupula increased in parallel with the surrounding medium, suggesting that both the indicator and K^+ penetrate into the cupula.

To precisely determine the absolute concentration of K^+ within the cupula under normal conditions (E3 saline), measured values were analyzed using chemical kinetics models. Specifically, fluorescence of saline external to the cupula was fit to a modified Hill equation,

$$\frac{F}{F_{max}} = \frac{[K^+]\,(1 - B_o)}{k_A + [K^+]} + B_o$$

where F is the fluorescence of the indicator, F_{max} is the fluorescence of the indicator at saturation, B_o represents the baseline fluorescence of the indicator normalized by F_{max}, k_A is the indicator binding affinity, and [K$^+$] is the K$^+$ concentration of the medium. The fluorescence of the indicator was taken as the measured fluorescence minus the fluorescence for the same region in the absence of the indicator. Fitting was performed using non-linear least squares optimization (Mathworks, MATLAB 2019b). The computed binding constants for IPG-4 were consistent with previously reported values (k_A= 20 ± 4 mM, mean ± S.E.M. (3)). This model of the concentration dependence of the indicator (k_A, B_o) was then applied to compute the K$^+$ concentration within the cupular matrix under normal conditions:

$$[K^+]_c = k_A \frac{F_c/F_{c,max} - B_o}{1 - F_c/F_{c,max}}$$

where here F_c represents the fluorescence of the indicator in the cupular matrix in E3 saline and $F_{c,max}$ is the fluorescence of the indicator in the same region with a saturating K$^+$ medium (60 mM). For this analysis, only the fluorescence of the cupular matrix in E3 saline and with a saturating K$^+$ medium are used. Any potential effects of elevated K$^+$ on the physiology of the neuromast would not be expected to modify these results, provided that these effects do not alter the chemical partitioning of the ion indicator between the external medium and cupular matrix. The difference between the K$^+$ concentration in the cupula and the surrounding medium was then compared to zero using a two-tailed one-sample t-test.

The Na$^+$ concentration was measured using a similar protocol with a different probe (10 µM ING-2 [Ion Biosciences] in HEPES-buffered E3, 5-95 NaCl for calibration, K_A=30 ± 10 mM (4), excitation: 488 nm, emission: 500-550 nm). To record the Ca^{2+} concentration, animals were first imaged in a medium containing a Ca^{2+} selective indicator (10 µM Fluo5N [Invitrogen] in HEPES-buffered E3, k_a = 20 ± 3 µM (5), excitation: 488 nm, emission: 500-550 nm), then the medium was replaced by saline solutions with varied Ca^{2+} concentrations (0-2 mM, prepared by varying CaCl$_2$, random order). The difference between the Ca^{2+} concentration in the cupula and medium was computed for 20 µM Ca^{2+} medium rather than E3 medium, since this provides a lower baseline and would be more sensitive to deviations. Similarly, to record the H$^+$ concentration, animals were imaged in neutral-pH medium with a selective probe (10 µM BCECF [Cayman Chemicals] in HEPES-buffered E3 [pH = 7.2], excitation: 496 nm, emission: 477-545 nm), then the medium was replaced by saline solutions with varied pH values (first increased to pH=8.4, then decreased to 4.0, prepared by titrating with NaOH or HCl, 5mM MES added to medium for solutions with pH < 6.8). Since BCECF is quenched, this calibration curve was fit to the Stern-Volmer equation instead of the Hill equation and F_{max} was taken as the fluorescence at the highest examined pH value, but calculations were otherwise similar. The Cl$^-$ concentration within the cupular matrix was measured using the fluorescent indicator MQAE (1 mM in HEPES-buffered E3). In order to provide excitation at the short UV wavelengths required by MQAE, imaging was performed using two-photon microscopy (custom-built system, Zeiss 20x/1.0 objective, Coherent Chameleon Vision II laser, 750 nm excitation, Chroma HQ480/40M emission filter). Since the MQAE could be visualized quickly penetrating through the cupula and to limit the potential for UV-induced damage, the indicator calibration was performed in a separate series of experiments without the animal (0-50mM KCl) rather than with the animal as above. To produce a calibration curve, the fluorescence at each Cl$^-$ concentration was normalized by the fluorescence recorded for saline with a Cl$^-$ concentration equal to E3 medium. The fluorescence measured in the cupula was then normalized by the fluorescence in the surrounding medium, and this value was compared to the calibration curve to calculate the concentration of Cl$^-$ in the cupula.

Membrane reversal potentials

The membrane reversal potentials for the MET channel of the lateral line hair cells in different extracellular salines were estimated using a modified constant field equation that includes the contributions of Ca^{2+} (modified GHK equation, (6, 7)). The examined extracellular concentrations were centered around the values for E3 medium, and the intracellular ionic composition was assumed to be similar to other neurons ($[Na^+]_{out}$ = 5 mM, $[Na^+]_{in}$ = 5 mM, $[K^+]_{out}$ = 0.17 mM, $[K^+]_{in}$ = 130 mM, $[Ca^{2+}]_{out}$ = 0.33 mM, $[Ca^{2+}]_{in}$ = 100 nM, 28°C, (8)). The relative permeabilities of MET channels were estimated based on measurements from hair cells in other species: $P(Ca^{2+})$ = 5, $P(K+)$ = 1.15, $P(Na^+)$ = 1 (9–11). For comparison, the reversal potential for selective chloride conductance was also estimated using the Nernst equation ($[Cl^-]_{in}$ = 10 mM, 28°C, (12)). The calculated reversal potentials were compared against the opening potential for the voltage-gated Ca^{2+} channels on the basolateral membrane (CaV1.3, estimated at -50mV, (13–16)).

Cupula diffusion experiments

Animals were prepared as in the cupula ionic composition experiments. We visualized the precise boundary of the cupula by immersing the animals in fluorescent polystyrene microspheres and allowing them to coat the cupula (200 nm, suncoast yellow, FSSY002, Bang Labs; 1:100 in HEPES-buffered E3 (17)). The permeability of the cupular matrix was measured by recording the penetration of a negatively-charged fluorophore (6-carboxyfluorescein; Sigma-Aldrich) into the cupula. The fluorophore (10 µM in HEPES-buffered E3) was loaded into a glass pipette (tip diameter: ~5 µm; Model P-97 Flaming/Brown Micropipette Puller, Sutter Instrument Co.) aimed ~20 µm away at the cupula. The pipette pressure was then rapidly increased by opening a valve attached to a pressure source (100 torr, Fluke Biomedical Instruments DPM1B), dye surrounded the cupula, and the change in fluorescence over time was recorded at the stereocilia level (Leica TCS SP5, HCX PL APO CS 63x/1.2 water objective, 20 frames/sec, excitation: 488 nm; emission: 500 - 550 nm). Values for F/F_{max} were computed by subtracting the fluorescence prior to dye release, and then normalizing by the maximum fluorescence following release. The time constant for the increase in dye fluorescence was fit to an exponential waveform

$$\frac{F}{F_{max}} = 1 - e^{-t/\tau}$$

where F_{max} is the maximum fluorescence, τ is the time constant, and t is time. Fitting was performed using non-linear least-squares fitting (Mathworks, MATLAB R2020b). The time constant was 1.6 $\pm$ 0.5 (s) for the cupula and 2.1 $\pm$ 0.8 (s) for the surrounding medium (mean $\pm$ SEM). Relative time constants were calculated as the ratio of the time constant in the cupula divided by the time constant in the surrounding medium for the same trial. Differences were identified by comparing this relative time constant to one using a two-tailed one-sample t-test.

Computational cupula diffusion model

Simulations of the fluorophore diffusion experiments were performed by modeling the cupula as a cylinder (13 µm diameter, 40 µm height, Fig. S1A, (17)) of uniform material with an isotropic diffusion coefficient. Since the pipette jet rapidly replaced the fluorophore solution at the periphery of the cupular during experiments, the fluorophore concentration was assumed to be uniform over the exposed surface of the cupula and increase following an exponential waveform with parameters estimated from the imaging data, see cupula diffusion experiments). Diffusion is a linear process and the absolute fluorophore concentration does not alter the dynamics, so the concentration was arbitrarily selected to ramp from zero to one. The cylinder was discretized

using an all-tetrahedral mesh and Fick's equation was solved for this geometry using a commercial finite element method solver (Comsol 6.0). A sensitivity analysis was performed to ensure that mesh density and time stepping were adequate. Although the central problem is axisymmetric, a 3-dimensional mesh was used as some sensitivity analyses included non-axisymmetric convective terms. This model was then solved for a logarithmic series of cupular matrix diffusion coefficients surrounding the value recorded for the fluorophore in free water (1×10^{-12} to 1×10^{-9} m^2/s, $D_{6CF} = 0.487 \times 10^{-9}$, (18)), and the predicted temporal profile of the fluorophore at the center of the cupula was calculated for each condition. The cupular diffusion coefficient was then estimated by comparing the time constants from these simulations to the time constants obtained from the imaging experiments.

Computational Nernst-Planck model

We performed a series of computational studies to determine how K$^+$ secretion at the apical surface of the neuromast would affect K$^+$ concentrations within the cupula. The cupula was modeled as a cylinder (13 µm diameter, 40 µm height, Fig. 1H left, (17)) immersed in an infinitely large electrolyte bath (hemi-spherical bubble with radius of 100 µm explicitly modeled, surrounding volume modeled using infinite element domain). The ion currents and concentrations within the cupula and surrounding medium were modeled using the full Nernst-Planck equations subject to the electroneutrality approximation and solved using a commercial finite element method multiphysics package (Comsol 6.0). This approach calculates ion movements due to both diffusion and electrical gradients, and the electrical gradients are updated based on ion movement and boundary conditions. The electrolyte included K$^+$, Na$^+$, and Cl$^-$ ions and the self-diffusion coefficients for each ion in the surrounding medium were taken from previously reported values (K$^+$: 1.89×10^{-9}, Na$^+$: 1.33×10^{-9}, Cl$^-$: 2.06×10^{-9} m^2/s, (19, 20)). The model was solved for two configurations: the most probable scenario in which the ion diffusion coefficients in the cupular matrix are equivalent to those in water, and a conservative model in which the diffusion coefficient of each ion was scaled down to match the lower bound of the 95% CI for the relative diffusion coefficient obtained in the 6-CF experiments (6.9% of free water). The electrical mobility of each species was estimated using the Nernst-Einstein relation. The model was solved using a steady-state axisymmetric system, the cupula and explicit medium domain were meshed using free triangular elements, the infinite element domain was meshed with mapped quadrilateral elements, and a sensitivity analysis was used to confirm that the mesh density was sufficient. The boundary conditions were set such that at infinity the electrical potential was zero and the ion concentrations were equal to those of E3 medium (0.17 mM K$^+$, 5 mM Na$^+$, 5.17 mM Cl$^-$), the surface of the body was impermeable to all ions, and the base of the cupula secreted K$^+$ ions at a fixed rate. Simulations were performed for a logarithmic series of K$^+$ secretion currents spanning a wide range ($1 \times 10^{-10} - 1 \times 10^{-6}$ A), and K$^+$ concentrations at the base of the cupula and in the surrounding medium were computed for each current value. Results were qualitatively similar for the water-like diffusion configuration and the conservative configuration with scaled down diffusion coefficients, although the conservative configuration yielded higher K$^+$ concentrations within the cupula as expected (reaching a K$^+$ concentration of 10.2 mM at the apical surface requires 56 nA for a diffusion coefficient equal to water, and 4.8 nA for a diffusion constant at the lower bound of the 95% confidence interval).

We used a similar approach to produce an order-of-magnitude estimate of the maximum sustainable Ca^{2+} current into an isolated hair cell in a reduced Ca^{2+} concentration environment. For these simulations, we used a 4-species model that included K$^+$, Na$^+$, Cl$^-$, and Ca^{2+}. Model parameters followed those of the prior model and assumed that the cupular matrix is similar to free water, with the Ca^{2+} self-diffusion coefficient taken from previously reported values (0.7806×10^{-9} m^2/s, (21)) and the Ca^{2+} concentration matched to the low-Ca^{2+} functional imaging

5

experiments (20 μM). Calcium was assumed to have a uniform flux through the stereocilia bundle, which was modeled as a flat patch with a 600 nm diameter at the neuromast base (22). Since this model examines ion diffusion through the surrounding water rather than ion transport through the apical membrane, it is expected to be minimally affected by the precise geometry of the stereocilia bundle. The model was solved for a range of Ca^{2+} current values, the resulting Ca^{2+} concentration at the center of the patch was calculated, and the maximum sustainable Ca^{2+} current was estimated as that which produced a zero Ca^{2+} concentration at the patch center. This approach is not explicitly dependent on the MET channel conductance or the hair cell membrane potential, as these properties are integrated within the Ca^{2+} current. Using this strategy, we calculated the maximum sustainable Ca^{2+} current to be 2.8 pA. This model examined current into an isolated hair cell with no adjacent active hair cells. To evaluate the sensitivity of these results to neighboring active hair cells, we performed a similar calculation examining the maximum sustainable Ca^{2+} into an entire neuromast. For these simulations, we conservatively assumed that the entire base of the neuromast drove a uniform Ca^{2+} flux (13 μm diameter patch, (17)). Here, the maximum sustainable Ca^{2+} current was estimated to be 61 pA for the entire neuromast, or 5.1 pA per hair cell assuming 12 hair cells per neuromast (23). This value is comparable to that estimated for an isolated hair cell, and suggests these results are not highly sensitive to the model assumptions.

Calcium imaging

We examined the responses of the lateral line hair cells to mechanical stimuli in environmental salines with varying ionic compositions. Larvae (5 -7dpf) expressed the membrane-localized fluorescent calcium indicator gCaMP6s-CAAX in hair cells (*myo6b:gCaMP6s-CAAX,* (24)), and were immobilized and imaged as described above (in HEPES-buffered E3). A glass bead (5 μm) attached to a piezoelectric transducer (30V300, Piezosystem Jena) was positioned approximately 10 μm anterior from the distal end of the neuromast kinocilia (25, 26). During each trial, a stimulus program (Clampex 10.1) controlled via a low-noise digitizer (Digidata 1440A) elicited three sweeps of sinusoidal movement (5 Hz) for 20 seconds, separated by 40s periods of inactivity. The first sweep was preceded by and the last sweep was followed by a 20s period of inactivity. The glass bead vibrated, deflecting the cupula in the anterior-to-posterior direction. Cupula deflection was monitored by measuring the displacement distance of the kinocilia tips (~10 μm). Mechanosensitive Ca^{2+} responses were measured within the hair cells (Leica TCS SP5 II, HCX PL APO CS 63x/1.2 water objective, 5 frames/sec, excitation: 488 nm, emission: 501 - 583 nm). Between trials, the perfusate bath was replaced using media with decreased total Ca^{2+} concentration (20 μM Ca^{2+}: HEPES-buffered E3 with reduced $CaCl_2$, or 0 μM Ca^{2+}: HEPES-buffered E3 with $CaCl_2$ replaced by equivalent concentration of $MgSO_4$). Preliminary experiments performed in medium containing EGTA (0.2 mM) yielded similar results to 0 μM Ca^{2+} trials, suggesting these solutions contained negligible residual calcium. Responses to stimuli were quantified by finding the mean fluorescence within manually selected regions of interest (ROI) for individual hair cells (ImageJ). Fluorescence values were then used to compute "ΔF/F" as

$$\Delta F/F = \frac{F - F_o}{F_o}$$

where F is the instantaneous fluorescence within the ROI and F_o is the mean fluorescence within the ROI prior to the stimulus onset. Responses were detected by comparing the time-average of the ΔF/F during stimulus periods to non-stimulus periods using a paired two-tailed t-test. Changes in response amplitude were identified by comparing the time-average during stimulus periods between treatment groups (20 μM Ca^{2+} and 0 μM Ca^{2+} medium) and the control (E3 medium) using a paired two-tailed t-test. Sample sizes were determined using a power analysis based on variances and effect sizes estimated from prior studies.

A similar protocol was used to examine the responses of hair cells to a calcium-activated chloride channel agonist. Baseline activity was recorded for 30 s in a freshwater medium (E3 saline), then perfused with Eact (50 µM in 0.1% DMSO final conc.; (27)). We monitored changes in fluorescence before, during, and after perfusion of Eact (0.8 frames/sec, excitation: 488 nm, emission: 500 nm - 600 nm). Relative changes in fluorescence were quantified using regions of interest around responsive hair cells. Mean ΔF/F during the 30 sec prior to Eact exposure was then compared to the mean response for 60 sec following Eact exposure using a paired two-tailed t-test.

We then examined the responses of hair cells to mechanical stimuli after exposure to a calcium-activated chloride channel antagonist. A wide tipped (~20 µm) glass pipette filled with freshwater media (HEPES-buffered E3 saline) connected to a pneumatic microinjector (PV 820 Pneumatic PicoPump, WPI) was positioned anterior to the neuromast. During each trial, freshwater media was ejected from the pipette for 5 seconds to deflect the kinocilia in the anterior-to-posterior direction (~10 µm), this was followed by a 40 s period without stimulus, and this was repeated three times. Mechanosensitive Ca^{2+} responses in control conditions (HEPES buffered E3 saline) were measured at the basal membrane of the hair cells (Zeiss VIS-IR 63x/1.0 water objective, 2 frames/sec, excitation: 488 nm, emission: 500-600 nm) on an upright microscope (Zeiss Z1 Examiner, Germany), mounted with a spinning disc head (CSU-X1, Yokogawa, Japan), and laser light source (LaserStack, 3i Intelligent Imaging Innovations, USA). We then repeated the experiment in T16A$_{inh}$-A01 (25 µM in 0.5% DMSO in HEPES buffered E3; (27)) and after a washout (HEPES-buffered E3). Changes in fluorescence were quantified using regions of interest around responsive hair cells (Suite2p). The mechanical stimulus produced noticeable increases in ΔF/F, with undershoot and shifts in baseline activity over the recording period were also apparent in some recordings (Fig. S5). Each response was quantified as the difference between the mean ΔF/F during the stimulus and the mean ΔF/F for the preceding 10 sec. The effect of blockade was determined by comparing this response between the between the control or washout and the treatment (T16A$_{inh}$-A01) groups using a paired two-tailed t-test.

Behavioral assays
The behavioral response of zebrafish larvae (5-7 dpf, AB strain) to mechanical stimuli was assessed using a custom-developed behavioral assay. This assay was conducted in an enclosure that maintains a constant internal temperature (28°C, using Fisher Scientific IsoTemp 6200 R28) and isolates experiments from ambient light and noise. Animals were transferred into a dish containing the experimental saline (38 mm diameter, 6 mm height) to incubate (20 min for all trials except neomycin, which incubated for 1 h), then transferred into the behavioral chamber and allowed to acclimate briefly (5 min) prior to experiments. The behavioral chamber was designed to operate as an oscillatory Couette cell, which produces shear stress in the fluid but not pressure waves (28). This chamber was laser cut from acrylic sheet and provided a cylindrical raceway (35 mm outer diameter, 25 mm inner diameter, filled to depth of 5 mm) that was suspended by flexible struts. These flexible struts functioned as a flexure bearing system, allowing oscillatory rotations of the raceway about the cylindrical axis while preventing translation or other rotations. Oscillatory rotations were driven using a fourth, rigid strut that was affixed with adhesive to the center dome of a speaker (Soberton SP-3114Y), which was connected to an audio amplifier (Adafruit 987, MAX98306). The chamber was diffusely illuminated from above with white light (ST-WP-5050-DL-RL, TheLEDLight.com) to maintain normal swimming behavior.

Stimulus generation was controlled via a custom-written MATLAB script (Mathworks, R2020b) and a data acquisition system (National Instruments, PCIe-6323). Each experiment consisted of a baseline activity recording period (300 s) followed by a series of 35 trials with stimuli. Each trial began with a 2 s mechanical stimulus (20 Hz, 5 amplitudes with 7 replicates

each, randomly ordered) followed by a randomized interstimulus interval (mean: 120 s, std. dev.: 20 s, min: 60 s, max: 180 s). The magnitude of the stimulus was calibrated by imaging the rigid strut of the raceway using a high-speed camera system (Phantom Miro 340, 200 fps, Samyang 1.4/85mm lens, 68 mm of extension tubes) and computing the displacement with sub-pixel precision using a custom-written MATLAB script. Reported stimulus amplitudes represent the displacement amplitude at the outer wall of the raceway.

The movement of the animals was continuously recorded and used to assess the response to the mechanical stimulus. A sheet of rear screen projection material (GooScreen BlackMax 1950) was positioned beneath the behavioral arena and illuminated with near-infrared light (850nm, ThorLabs 850L3). Animals were then imaged using a NIR-sensitive camera positioned above the arena (30 frames/sec, Point Grey GS3-U3-41C6NIR) equipped with a NIR-transmissive lens (Schneider 50mm Xenoplan, 1001976) and visible light blocking filter (Lee Filter #87). During each stimulus period, a small NIR LED positioned within the field of view was automatically illuminated, and this light was used to synchronize the stimuli with the recorded video to within one frame. The position of the larvae in each image frame was calculated using previously developed MATLAB scripts (https://bitbucket.org/jastrother/larval_proving_grounds).

The response to each stimulus was scored based on the induced change in the swimming speed of the larvae. In order to quantify each response in a way that was independent of the average swimming speed of the animal, each trial was scored as a response if the stimulus elicited a change in the swimming speed that fell outside of the 95% confidence interval computed for similar stimulus-free periods. Specifically, the average swimming speed of the animals was computed for 3 time windows: a first reference window (500 ms duration, ending 10 s prior to the stimulus), a second reference window (500 ms duration, ending 5 s prior to the stimulus), and a response window (500 ms duration, starting with the stimulus). The difference between the first and second reference window was aggregated and used to compute the cumulative probability distribution of the spontaneous swimming speed change during a stimulus-free period for each individual. The difference between the second reference window and the response window was compared to this distribution, and each trial was marked as a response if it fell below the 2.5% percentile or above the 97.5% percentile. Since this approach yields an expected false positive rate of 5%, the calculated response probabilities were offset by the same amount.

Differences in the response probability between experimental and control groups were detected with two different statistical analyses. First, multinomial probit regression was used to implement an omnibus test that detects differences between the experimental and control groups while integrating information across stimulus intensities (Mathworks, MATLAB R2020b). Second, pairwise differences between the experimental and control groups at specific stimulus intensities were detected using Fisher's exact test with false discovery rate control implemented using the Benjamini-Hochberg procedure (Mathworks, MATLAB R2020b). Plots include error bars representing S.E.M. values, where the variance was calculated using the properties of binomial distribution [p (1-p)]. Sample sizes were determined using a power analysis based on variances and effect sizes estimated from prior studies.

The following conditions were examined: "HEPES-buffered E3 medium" (5 mM NaCl, 0.17 mM KCl, 0.33 mM $CaCl_2$, 0.33 mM $MgSO_4$, 1 mM HEPES, titrated to pH 7.2-7.4 with HCl/NaOH), "200 µM Neomycin medium" (200 µM neomycin sulfate in HEPES-buffered E3 medium), "50 µM niflumic acid" (50 µM niflumic acid in HEPES-buffered E3 medium with 0.05% DMSO), "3x Ionic Strength medium" (NaCl and KCl increased 3x relative to E3: 15 mM NaCl, 0.51 mM KCl, 0.33 mM $CaCl_2$, 0.33 mM $MgSO_4$, 1 mM HEPES, titrated to pH 7.2-7.4 with HCl/NaOH), "20x Ionic Strength medium" (NaCl and KCl increased 20x relative to E3: 100 mM NaCl, 3.4 mM KCl, 0.33 mM $CaCl_2$, 0.33 mM $MgSO_4$, 1mM HEPES, titrated to pH 7.2-7.4 with

HCl/NaOH), "0.8 mM Cl⁻ medium" (replace NaCl with Na-Gluconate in E3: 5 mM Na-Gluconate, 0.17 mM KCl, 0.33 mM $CaCl_2$, 0.33 $MgSO_4$, 1 mM HEPES, titrate to pH 7.2-7.4 with citric acid/NaOH), "16 mM Cl⁻ medium" (major cations matched to E3, approximately isosmotic to 3x Ionic Strength medium: 5mM NaCl, 10.3 mM NMDG-Cl, 0.17 mM KCl, 0.33 mM $CaCl_2$, 0.33 $MgSO_4$, 1mM HEPES, pH 7.2-7.4), "104 mM Cl⁻ medium" (major cations matched to E3, approximately isosmotic to 20x Ionic Strength medium: 5 mM NaCl, 98.22 mM NMDG-Cl, 0.17 mM KCl, 0.33 mM $CaCl_2$, 0.33 mM $MgSO_4$, 1mM HEPES, titrated to pH 7.2-7.4 with HCl/NaOH), and "20 µM Ca^{2+} medium" (replace Ca^{2+} with Mg^{2+} in E3: 5 mM NaCl, 0.17 mM KCl, 20 µM $CaCl_2$, 0.31 mM $MgCl_2$, 0.33 mM $MgSO_4$, 1 mM HEPES, titrated to pH 7.2-7.4 with HCl/NaOH). The HEPES-buffered E3 medium served as the control for all experimental groups, and control trials were run in parallel with experimental trials. Since the responses from control trials exhibited very little inter-clutch variation, data from control trials was pooled when performing statistical analyses. At least 3 clutches of embryos were used for all conditions, and parents were randomly selected from a genetically diverse population.

Analysis of transcriptomic data
In order to identify gene products that may be contributing to the mechanotransduction process, we conducted a survey of previously published lateral line neuromast scRNA-seq data (29). A MATLAB script (Mathworks, R2020B) was written that performed the following steps: cells that express the hair cell marker *tmc2b* were selected, the transcripts expressed by each selected cell were filtered to include genes annotated with a relevant list of ontology terms ("ion transport", "ion channel activity", "gpcr activity", "chemical synaptic transmission", "hormone activity", "neuropeptide hormone" for *Danio rerio* in AmiGo2, (30) and a manually curated listed of similar genes not captured in the gene ontology database (based on searches of zfin.org, (31)), and the resulting list was then reviewed to identify genes with known anion efflux activity. This analysis was performed exclusively for hypothesis generation. To avoid issues with pseudoreplication, further examination of the genes of interest was performed in independent experiments (e.g., *in situ* hybridization) rather than a statistical analysis of the same transcriptome dataset.

In situ hybridization
The expression of *ano2b* was examined using HCR RNA-FISH (32) following protocol based on the manufacturer's directions. Briefly, larvae (AB strain, 4 dpf) were cold anesthetized and fixed with 4% PFA in PBS (overnight at 4°C), washed with PBS (3x, 5 min, room temperature [RT]), dehydrated with a PBS/MeOH series (75/25%, 50/50%, 25/75%, 0/100%, 5 min each at RT), frozen (1 hr at -20°C), rehydrated with a MeOH/PBST series (75/25%, 50/50%, 25/75%, 0/100%, 5 min each at RT, PBST: PBS with 0.1% Tween 20), incubated in hybridization buffer (20 min at 37°C), hybridized with *ano2b* probes (20 nM, overnight at 37°C), washed with probe wash buffer (4x, 15 min, 37°C), washed with 5X SSCT (2x, 5 min, RT; SSCT: SSC with 0.1% Tween 20), incubated in amplification buffer (30 min, RT), incubated with snap-cooled amplifiers in amplification buffer (60 nM each, 18 h, RT), washed with 5X SSCT (2x 5 min, 2x 30 min, 1x 5 min, RT), labeled with DAPI (30 min, 1 µM in 5X SSCT, RT), and imaged on a confocal microscope (Leica TCS SP5, HCX PL APO CS 63x/1.2 water objective for hair cells, HC PL Fluotar 20x/0.5 objective for others, DAPI: excitation = 405 nm, emission = 415 - 485 nm, AlexaFluor 647: excitation = 633 nm, emission = 695 - 765 nm). Images were collected of superficial neuromasts, olfactory epithelium, and the CNS. Images were also collected from randomly selected regions along the trunk adjacent to superficial neuromasts, in order to verify that the observed labeling of superficial neuromasts was not a product of non-specific surface labeling.
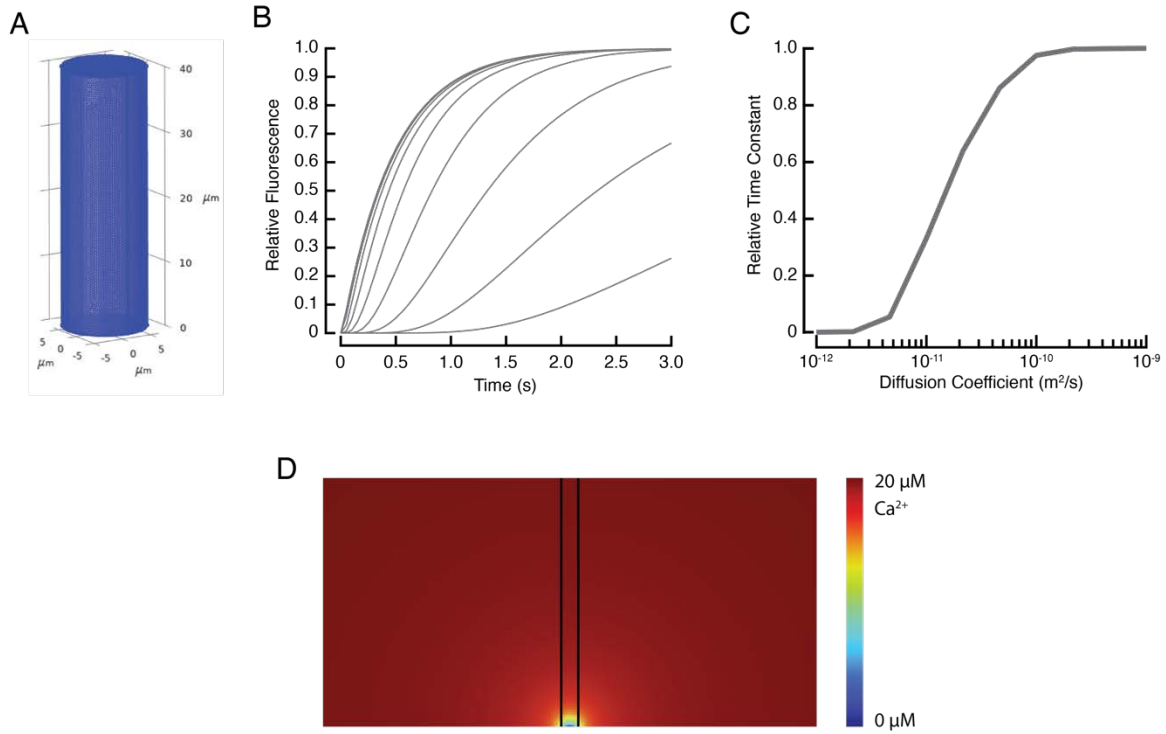
Fig. S1: Computational simulations supporting cupula diffusion and calcium imaging experiments. (A-C) Results from simulations of diffusion experiments. (A) Mesh used for finite element model. (B) Simulated time series for a position just above the base of the cupula (8 μm) for a range of diffusion coefficients (1×10^{-12}, 2.15×10^{-12}, 4.64×10^{-12}, 1×10^{-11}, 2.15×10^{-11}, 4.64×10^{-11}, 1×10^{-10}, 2.15×10^{-10}, 4.64×10^{-10}, 1×10^{-9} m²/s). (C) Simulated relative time constant as a function of the modeled diffusion coefficient. Comparison of experimental and modeling results indicate that the diffusion of the charged fluorophore 6-CF through the cupular matrix is similar to that through water ($0.034 \times 10^{-9} - 0.487 \times 10^{-9}$ m²/s, 6.9%-100% of water, 95% CI), with the lower bound of the estimate limited by the achievable dye injection speed of the experimental apparatus. (D) Results from simulations examining maximum sustainable Ca^{2+} current into an isolated hair cell in a reduced Ca^{2+} extracellular saline (20 μM). Image shows the distribution of Ca^{2+} in the extracellular space above the apical surface of a hair cell for an inward current of 2.5pA. The width of the apical surface of the hair cell is represented by vertical black lines. These lines do not demarcate any change in the boundary conditions within the extracellular fluid.
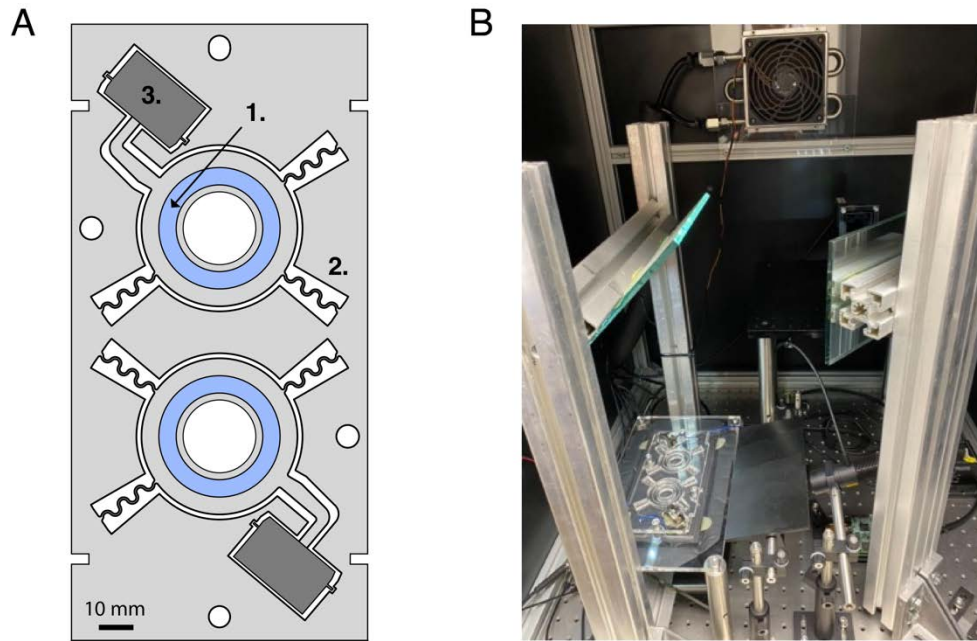
Fig. S2: Apparatus used for behavioral assays. (A) Outline of the behavioral arena, showing circular racetrack in which larva swims [1], which is suspended by flexure bearings [2] and driven by a speaker [3]. Each apparatus contains two chambers that are operated in parallel. (B) Image of behavioral assay in a temperature controlled enclosure.
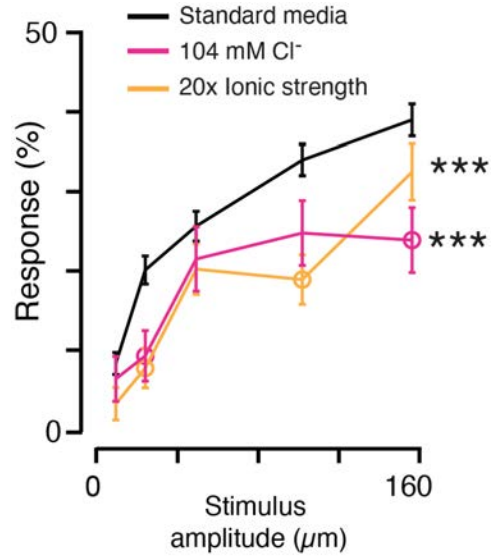
Fig. S3: Zebrafish larvae display reduced lateral line sensitivity in environmental saline solutions with higher ionic strength. The response probability of zebrafish larvae to mechanical stimuli of different intensities in various environmental saline solutions, as measured using the oscillatory Couette behavioral assay. Asterisks indicate statistically significant differences integrated across stimulus intensities (*p<0.05, **p<0.01, ***p<0.001), open circles represent significant pairwise comparisons (p<0.05), and results are shown as mean ± SEM.
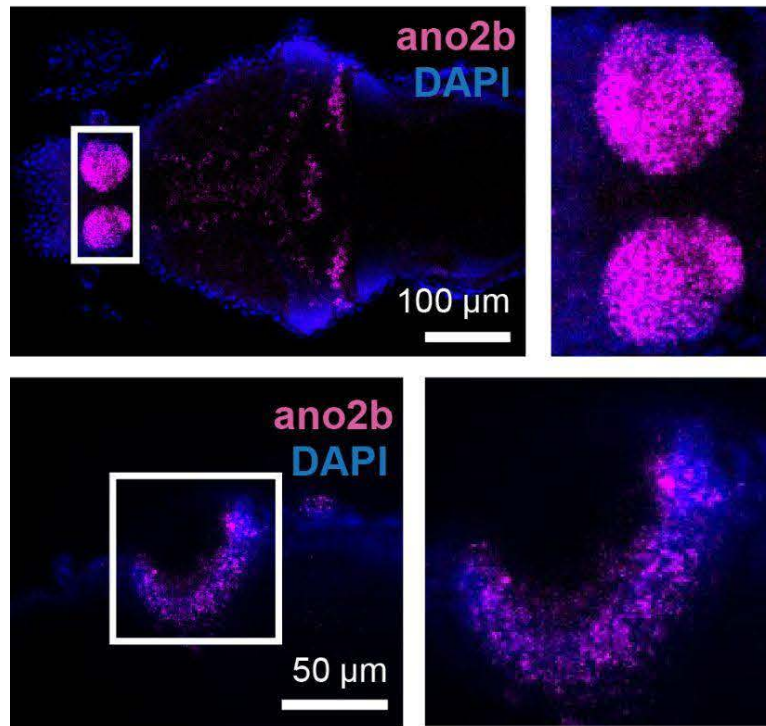
Fig. S4. *In situ* hybridization for *ano2* labels the dorsal habenula (top, magnified right) and the olfactory epithelium (bottom, magnified right).
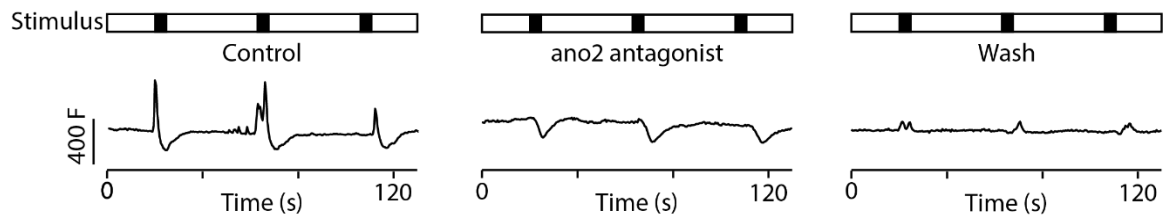
Fig. S5. Full time series of a representative hair cell's calcium response to cupula deflection while bathed in standard media (control; left), an Ano2 antagonist (25 μM T16A$_{inh}$-A01; middle), and following washout (right).

SI References

1. C. Nusslein-Volhard, R. Dahm, *Zebrafish* (OUP Oxford, 2002).
2. E. T. Lunsford, J. C. Liao, Activity of Posterior Lateral Line Afferent Neurons during Swimming in Zebrafish. *JoVE (Journal of Visualized Experiments)*, e62233 (2021).
3. P. S. Rana, *et al.*, Calibration and characterization of intracellular Asante Potassium Green probes, APG-2 and APG-4. *Anal Biochem* **567**, 8–13 (2019).
4. O. Iamshanova, P. Mariot, N. Prevarskaya, Comparison of fluorescence probes for intracellular sodium imaging in prostate cancer cell lines. *European Biophysics Journal* **45**, 765–777 (2016).
5. A. A. Kabbara, D. G. Allen, The use of the indicator fluo-5N to measure sarcoplasmic reticulum calcium in single muscle fibres of the cane toad. *J Physiol* **534**, 87–97 (2001).
6. C. A. Lewis, Ion-concentration dependence of the reversal potential and the single channel conductance of ion channels at the frog neuromuscular junction. *The Journal of Physiology* **286**, 417–445 (1979).
7. L. Y. Jan, Y. N. Jan, Properties of the larval neuromuscular junction in Drosophila melanogaster. *The Journal of Physiology* **262**, 189–214 (1976).
8. J. Olt, S. L. Johnson, W. Marcotti, In vivo and in vitro biophysical properties of hair cells from the lateral line and inner ear of developing and adult zebrafish. *The Journal of Physiology* **592**, 2041–2058 (2014).
9. B. Pan, *et al.*, TMC1 and TMC2 Are Components of the Mechanotransduction Channel in Hair Cells of the Mammalian Inner Ear. *Neuron* **79**, 504–515 (2013).
10. B. Pan, *et al.*, TMC1 Forms the Pore of Mechanosensory Transduction Channels in Vertebrate Inner Ear Hair Cells. *Neuron* **99**, 736-753.e6 (2018).
11. E. A. Lumpkin, R. E. Marquis, A. J. Hudspeth, The selectivity of the hair cell's mechanoelectrical-transduction channel promotes Ca^{2+} flux at low Ca^{2+} concentrations. *Proc. Natl. Acad. Sci. U.S.A.* **94**, 10997–11002 (1997).
12. J. Glykys, *et al.*, Local impermeant anions establish the neuronal chloride concentration. *Science* **343**, 670–675 (2014).
13. A. Brandt, D. Khimich, T. Moser, Few CaV1.3 Channels Regulate the Exocytosis of a Synaptic Vesicle at the Hair Cell Ribbon Synapse. *J Neurosci* **25**, 11577–11585 (2005).
14. J. Platzer, *et al.*, Congenital deafness and sinoatrial node dysfunction in mice lacking class D L-type Ca2+ channels. *Cell* **102**, 89–97 (2000).
15. I. Putzier, P. H. M. Kullmann, J. P. Horn, E. S. Levitan, Cav1.3 channel voltage dependence, not Ca2+ selectivity, drives pacemaker activity and amplifies bursts in nigral dopamine neurons. *J Neurosci* **29**, 15414–15419 (2009).
16. W. Xu, D. Lipscombe, Neuronal Ca(V)1.3alpha(1) L-type channels activate at relatively hyperpolarized membrane potentials and are incompletely inhibited by dihydropyridines. *J Neurosci* **21**, 5944–5951 (2001).
17. W. J. Van Trump, M. J. McHenry, The morphology and mechanical sensitivity of lateral line receptors in zebrafish larvae (Danio rerio). *Journal of Experimental Biology* **211**, 2105–2115 (2008).
18. E. M. Kramer, N. L. Frazer, T. I. Baskin, Measurement of diffusion within the cell wall in living roots of Arabidopsis thaliana. *Journal of experimental botany* **58**, 3005–3015 (2007).
19. E. Hawlicka, Self-diffusion of sodium, chloride and iodide ions in acetonitrile-water mixtures. *Zeitschrift für Naturforschung A* **42**, 1014–1016 (1987).
20. A. M. Friedman, J. W. Kennedy, The self-diffusion coefficients of potassium, cesium, iodide and chloride ions in aqueous solutions1. *Journal of the American Chemical Society* **77**, 4499–4501 (1955).
21. Wang, Jui, Tracer-diffusion in liquids. IV. Self-diffusion of calcium ion and chloride ion in aqueous calcium chloride solutions. *J. Am. Chem. Soc.* **75**, 1769--1770 (1953).
22. M. Holmgren, *et al.*, Mechanical overstimulation causes acute injury and synapse loss followed by fast recovery in lateral-line neuromasts of larval zebrafish. *eLife* **10**, e69264 (2021).
23. K. C. Newton, *et al.*, Lateral line ablation by ototoxic compounds results in distinct rheotaxis profiles in larval zebrafish. *Commun Biol* **6**, 1–15 (2023).

24.	Q. Zhang, *et al.*, Synaptically silent sensory hair cells in zebrafish are recruited after damage. *Nature communications* **9**, 1–16 (2018).
25.	M. Haehnel-Taguchi, O. Akanyeti, J. C. Liao, Afferent and motoneuron activity in response to single neuromast stimulation in the posterior lateral line of larval zebrafish. *J Neurophysiol* **112**, 1329–1339 (2014).
26.	D. A. Skandalis, E. T. Lunsford, J. C. Liao, Corollary discharge enables proprioception from lateral line sensory feedback. *PLoS Biol* **19**, e3001420 (2021).
27.	W. Namkung, Z. Yao, W. E. Finkbeiner, A. S. Verkman, Small-molecule activators of TMEM16A, a calcium-activated chloride channel, stimulate epithelial chloride secretion and intestinal contraction. *The FASEB Journal* **25**, 4048–4062 (2011).
28.	H. Lamb, *Hydrodynamics* (Dover, 1945).
29.	M. E. Lush, *et al.*, scRNA-Seq reveals distinct stem cell populations that drive hair cell regeneration after loss of Fgf and Notch signaling. *Elife* **8**, e44431 (2019).
30.	 The Gene Ontology resource: enriching a GOld mine. *Nucleic acids research* **49**, D325–D334 (2021).
31.	Y. M. Bradford, *et al.*, Zebrafish Information Network, the knowledgebase for Danio rerio research. *Genetics* **220**, iyac016 (2022).
32.	H. M. Choi, *et al.*, Third-generation in situ hybridization chain reaction: multiplexed, quantitative, sensitive, versatile, robust. *Development* **145**, dev165753 (2018).